



Directional fatigue behaviour of maraging steel grade 300 produced by laser powder bed fusion

Klas Solberg^{*}, Even Wilberg Hovig, Knut Sørby, Filippo Berto

Institutt for maskinteknikk og produksjon, NTNU, Trondheim, Norway

ARTICLE INFO

Keywords:

Additive manufacturing
Surface roughness
Defects
Directional fatigue
18Ni300 maraging steel

ABSTRACT

Surfaces of metals produced by additive manufacturing (AM) are known to be rough and populated with defects, this is, in particular, true for downward-facing (down-skin) surfaces. When dealing with the fatigue of as-built surfaces produced by AM, fatigue is typically initiating from surface defects. In this work, the fatigue behaviour of maraging steel grade 300 (18Ni300) produced by laser beam powder bed fusion (PBF-LB) is investigated. Fatigue initiation from surfaces built both up- and down-skin are investigated. This is done by using specimens where all surfaces are machined, except the one at interest. Specimens were built in 10 orientation ranging from 0° (horizontal, up-skin) to 135° (down-skin). The surface roughness was measured for all orientations; high surface roughness was found for down-skin surfaces while wavy surfaces were found for up-skin surfaces. The fatigue behaviour was found to be correlated to the build orientation and the surface roughness.

1. Introduction

Additive manufacturing (AM) offers new possibilities in terms of design freedom, lead time and cost reductions [1–3]. Nevertheless, the materials often contain defects deriving from the manufacturing process that are reducing the mechanical performance [4,5]. Typical defects are high surface roughness, lack of fusion, porosity, residual stresses and distortions [5–8]. In addition to this, the microstructure is often anisotropic, as a result of the steep thermal gradients in the building process [5]. There are several approaches when designing parts for AM, in some cases, parts are produced near-to-net shape and fully post-processed with machining and heat treatment. This is done to remove defects and achieve the highest possible quality while keeping the costs low by reducing material usage and the amount of tooling. In other cases, geometric complexity, only possible to be achieved by the AM process, is desired in the final design. In this case, it might be impossible to perform machining, and designers are forced to accept the presence of the rough and defect populated as-built (AB) surfaces.

The fatigue behaviour is in particularly sensitive to the above-mentioned defects deriving from the AM process. Many of the materials that are popular in metal AM have high strength and hardness, e.g. Inconel 718, Ti6Al4V, 18Ni300 and 17-4PH steel. From conventionally manufactured metals, high tensile strength and hardness are often correlated to a high notch sensitivity in fatigue loading [9]. In the AB

state, fatigue usually initiates from the rough surface or defects in the surface region [10]. By machining the surfaces, the surface defects are removed, and fatigue initiates from internal defects such as lack of fusion regions or pores [11]. Machining usually enhances the fatigue life, the same is true for chemical etching and other processes that can be used to remove surface defects [12]. Further enhancement of the fatigue behaviour can be achieved by performing hot isostatic pressing, where defects that are not open to a free surface can be closed [13,14]. In addition to these "geometry altering" post-processing methods, heat treatments are used to alter the microstructure. The heat treatments are specific to each alloying system [15], and can also be tailored to the specific AM processes [16].

Maraging steel grade 300 (18Ni300) is one of the alloying systems where mechanical performance can be enhanced by heat treatment. Maraging steel is a FeNi-based alloy with a dominating martensitic microstructure strengthened by precipitation hardening. The martensite in maraging steel is not caused by a high carbon content (like in many other tool steel) but instead by a high Ni-concentration [17]. The lack of carbon leads to good weldability, which makes the material a good candidate for AM [18,19,17,20].

Becker and Dimitrov [21] studied the Fatigue Crack Growth (FCG) of PBF-LB/18Ni300. The study included the effect of crack growth orientation (i.e. parallel and perpendicular to the build layers) and the effect of heat treatment. Faster FCG rates were observed for the AB conditions

^{*} Corresponding author.

E-mail address: klas.solberg@ntnu.no (K. Solberg).

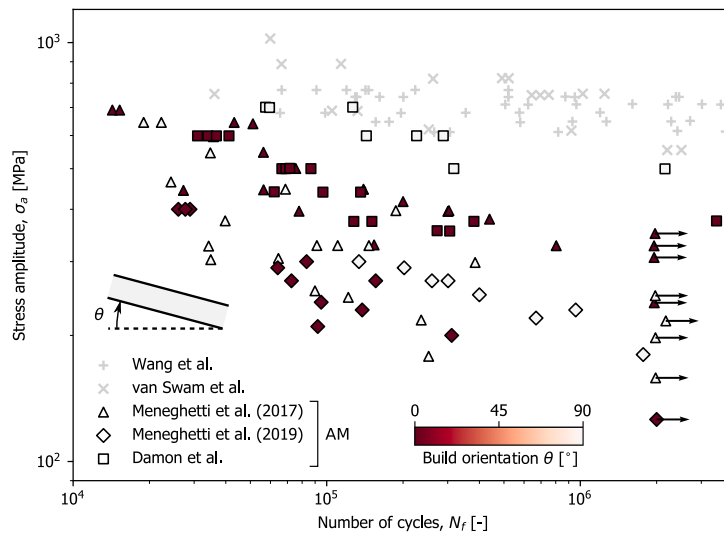


Fig. 1. Comparison of fatigue data from the literature. Wang et al. [22] van Swam et al. [23], Meneghetti et al. (2017) [24], Meneghetti et al. (2019) [26] and Damon et al. (PBF-LB) [27]. All fatigue data were tested at $R = -1$. Build angles are reported using the conventions of the current article: 0° - horizontal, 90° - vertical..

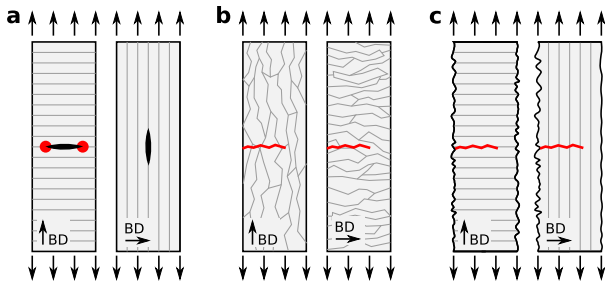


Fig. 2. Different features affecting the directional fatigue behaviour of AM metals. (a) orientation of defects, (b) microstructural anisotropy: orientation of columnar grains and (c) surface roughness dependent on surface orientation. Build directions indicated by BD.

when comparing them to the HT condition. The HT condition displayed the same FCG behaviour for both directions, which also coincided with the FCG for the wrought material. In the AB condition, faster FCG rate was observed parallel to the build layers than for perpendicular to the build layers. The uniaxial fatigue behaviour of AM 18Ni300 has also been studied; a collection of AM 18Ni300 fatigue data from the literature is shown in Fig. 1, compared to fatigue data of vacuum melted 18Ni300 [22,23]. The best fatigue performance is obtained in the

vacuum melted condition, while the AM studies displayed reduced performance. Concerning the directional fatigue behaviour of the AM materials, conflicting results have been reported. Meneghetti et al. [24] found higher fatigue life for the horizontal orientation than the vertical orientation. Crococo et al. [25] found similar fatigue performance for both horizontal and vertical orientations for bending fatigue. While Meneghetti et al. [26] and Damon et al. [27] found that vertical specimens outperformed horizontal specimens.

Dealing with the directional fatigue behaviour of AM metals, several explanations are given for differences in the fatigue properties. The three most usual explanations are illustrated in Fig. 2; The orientation of internal defects, the orientation of the microstructure and the surface roughness variations based on the surface orientations. Lack of Fusion (LoF) is one example of build direction-dependent internal defects. LoF defects are planar-like regions which have not been properly fused. As LoFs are planar-like defects, they are most critical when loading is occurring parallel to the build direction [28]. The microstructure of AM metals are in many cases anisotropic due to columnar grain growth parallel to the build direction [29]. When loading occurs parallel to the build direction, the fatigue crack needs to propagate through several grain boundaries than when loading occurs normal to the build direction, this is illustrated in Fig. 2b. Riemer et al. found that the threshold stress intensity factor (for fatigue crack initiation) was higher for 316L built in the vertical orientation than in the horizontal orientation [30], and reasoned for this by stating that the fatigue crack needed to propagate

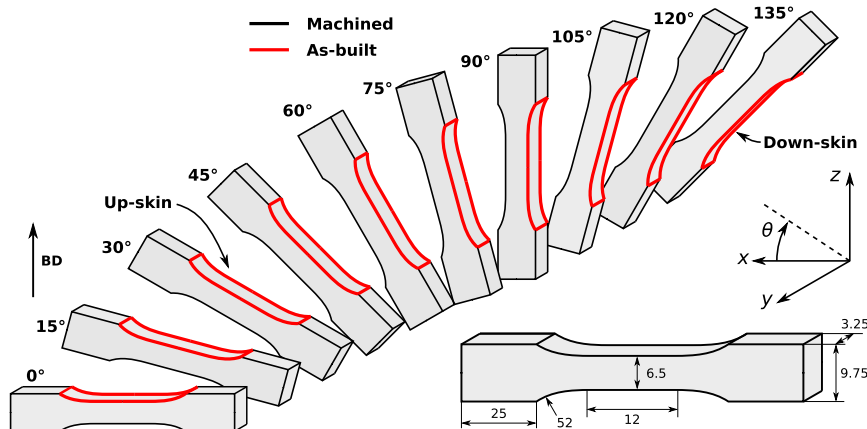


Fig. 3. Specimen orientations and dimensions. BD indicates the build direction.

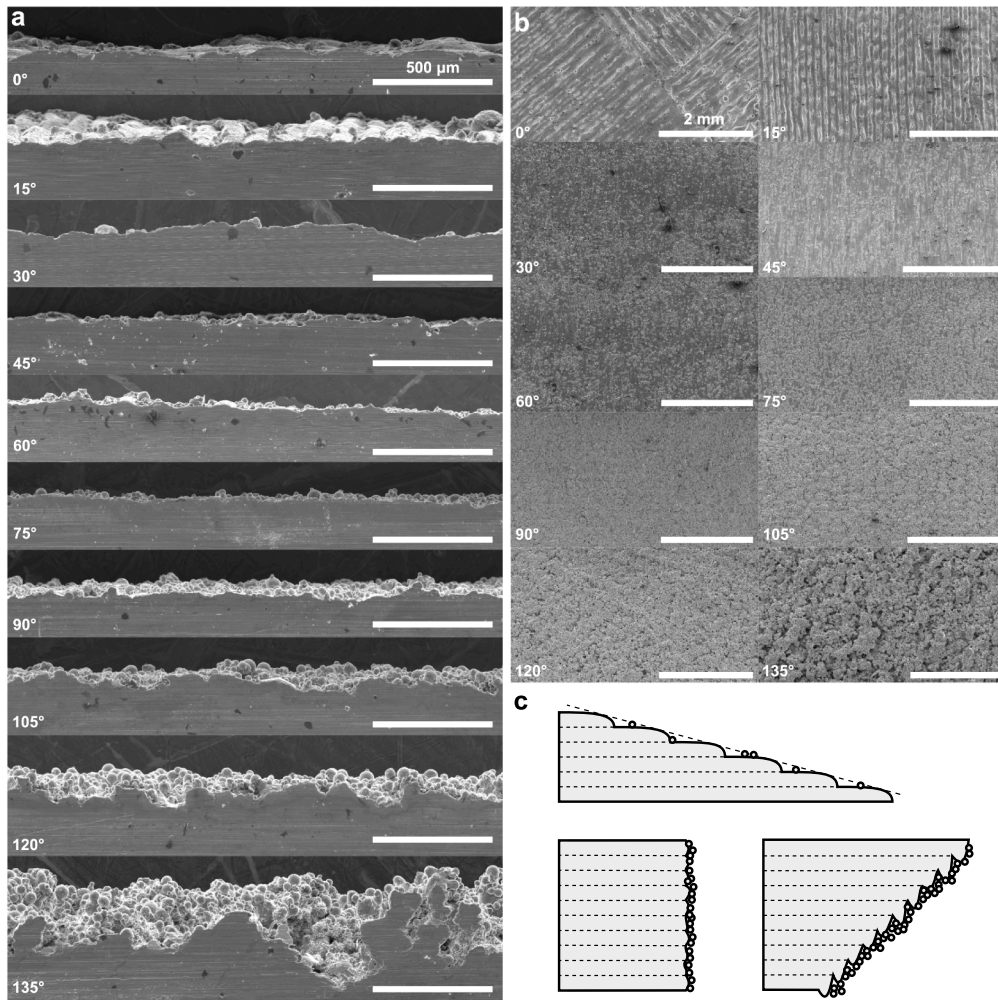


Fig. 4. SEM of surface conditions of specimens. (a) machined cross section (b) as-built surface (c) Schematic illustration of the different surface conditions.

through several grain boundaries. Dealing with uniaxial fatigue behaviour, the research usually shows that the fatigue life is higher for specimens built in the horizontal orientation [31,26,32]. The surface roughness and morphology are also dependent on the build orientations. Typically, down-skin surfaces (i.e. surfaces facing downwards) display higher surface roughness than up-skin surfaces (i.e. surfaces facing upwards). The valleys in the surface roughness profile act as stress risers, making them prone to fatigue initiation. Due to this, the main trend is that when the directional fatigue behaviour is assessed with an as-built surface, fatigue initiates from the down-skin region and not the up-skin region.

The goal of the present work is to evaluate directional fatigue behaviour of PBF-LB/18Ni300 maraging steel and in particular the fatigue behaviour of up- and down-skin surfaces. To do this, a new test specimen is proposed, where all sides of the specimens are machined except one side. Specimens were printed near-to-net shape for different orientations and then machined. To simplify the test scheme, one load level is selected for all the specimens. The fracture surfaces and the surface roughness profiles were investigated. Further, the porosity and microstructure were analyzed. Finally, the fatigue data are discussed in terms of variations in surface conditions and dimensional tolerances.

2. Methods

The specimen geometry is based on ASTM E466-15; Specimens with tangentially blended fillets between a uniform cross-section, the dimensions are shown in Fig. 3. The specimens were built in 10 different

orientations relative to the build platform, from 0° to 135° with steps of 15°. Three specimens were built in each orientation. The specimens were built in a Concept Laser system using a quadratic island strategy of 5 mm × 5 mm islands. The islands had an angular shift of 45° for each layer in addition to a 1 mm xy-shift in the island locations. The perimeter of each layers was scanned with a single contour track. The hatch spacing of the contour track was the same as the volume hatch. The same parameters were used for up-skin and down-skin surfaces. A laser power of 180 W, hatch spacing of 105 μm, scan velocity of 650 mm/s and a layer thickness of 30 μm was used as process parameters. Support structures were used for all down-skin surface except the surfaces left in the AB condition. The support type used was 'block' [33], with a wall thickness of 0.1 mm (one laser line) and a hatching on 1.5 mm between the walls in x- and y-direction. The specimens were heat-treated by direct aging at 500 °C for 5 h prior to removing them from the build platform and machining them.

To be able to observe the fatigue behaviour of the up-skin surfaces, one surface was left in the AB condition, as shown in Fig. 3. First, both sides of the specimens were ground to avoid distortion problems which have been observed for the same material and manufacturing processes [26]. After grinding, the specimens were machined on all sides except one surface.

The fatigue testing was done using a loading ratio $R = 0$ and a frequency of 30 Hz on an MTS servohydraulic system with a 50 kN load cell. To see the influence of the different build orientations and surface conditions without generating full SN-curves for each orientation, one load level was selected for the tests. The load level was based on

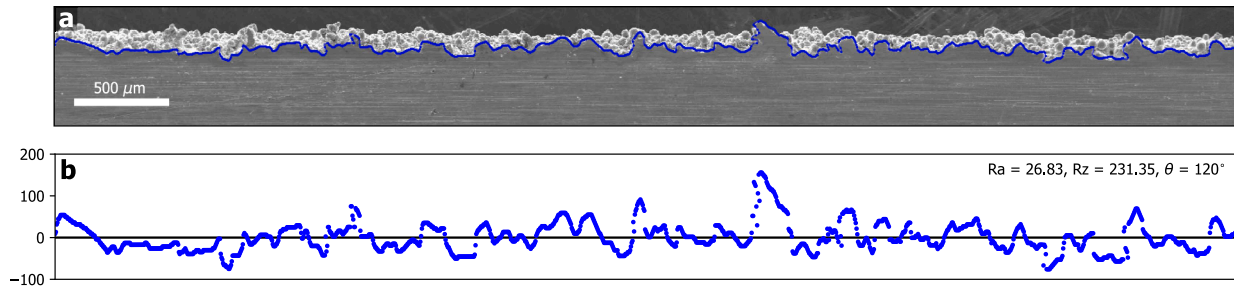


Fig. 5. Example of extraction and calculation of surface roughness parameters in python. (a) SEM with surface profile highlighted, (b) detected points used for calculation, note that Eq. (1) uses equally spaced points in the x-direction, which corresponds to the pixels in the SEM image.

experimental data on the same alloy from Meneghetti et al. [26] and on some initial trial and error testing of specimens with mistakes in the machining. The load level was determined to correspond to a stress range of 500 MPa, which results in fatigue failures around $\sim 10^5$ cycles. The gauge sections of all the specimens were measured with a caliper before testing.

A Scanning Electron Microscope (SEM) was used for analysing the fracture surfaces and for capturing the morphology of the as-built surfaces. Furthermore, the surface roughness of the as-built surfaces was calculated by extracting the surface profiles as lines in the software Inkscape then importing and processing them in python¹. Two different surface roughness parameters were calculated; the arithmetic mean deviation, R_a , and the maximum height of the profile, R_z . The arithmetical mean deviation of the assessed profile is given by

$$R_a = \frac{1}{n} \sum_{i=1}^n |y_i| \quad (1)$$

and the maximum height of the profile given by

$$R_z = |\max_i y_i| - |\min_i y_i|. \quad (2)$$

Where y_i is the distance from the mean line of n equally spaced points at the i^{th} data point. The mean line was calculated by linear regression using `numpy.polyfit`.

The porosity of the material was determined from optical micrographs of polished cross-sections. The micrographs were analysed by a python script using the `cv2.THRESH_BINARY`² threshold filter. The threshold was set so that the porosity was captured and scratches and other irregularities were ignored. The microstructure was investigated in SEM, by Back Scattered Electron (BSE) analysis. Before BSE, oxide suspension polishing was done with a particle size of 0.25 μm . Vickers hardness (1 kg) were measured on a Mitutoyo MicroWiZhard system.

3. Results

3.1. Surface roughness

The AB surfaces were investigated by SEM and are shown in Fig. 4. The side-view of the machined surfaces are shown in Fig. 4a and the view normal to the AB surfaces are shown in Fig. 4b. Fig. 4b shows that for the horizontal specimens (0°), the hatching strategy is visible. For low angles (15° – 60°), the different build layers are visible, displaying the staircase effect (see e.g. Fig. 4a 15°) which is characteristic for AM [34]. The surfaces built close to the vertical orientation displays a general roughness, which increases as the surface turns to down-skin. In the down-skin surfaces, the surfaces have increasingly higher roughness and

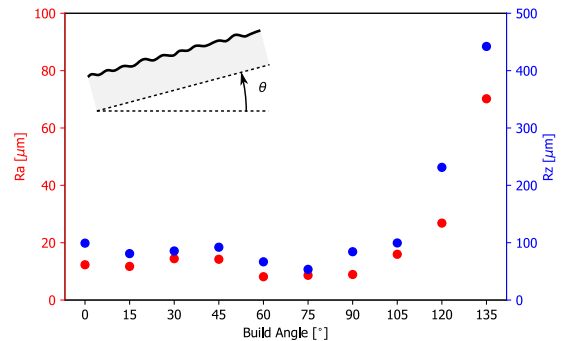


Fig. 6. Correlation between surface roughness (from SEM) and build angle.

high amounts of particles attached. It should be noted that the sharpness of the valleys of the surface in e.g. 135° are not high compared to what has been observed in other works where the melt pool geometry seems to directly dictate the surface morphology and create sharp corners [10].

Based on the SEMs in Fig. 4a and b, three main surface conditions can be identified:

- (i) for angles close to zero the stair-case effect is observed. In 0° the hatching pattern is visible and from 15° – 45° the stair-case effect is observed with an increased amount of attached powder particles as the angle increases.
- (ii) For angles between 45° and 90° a general surface roughness is observed, with an increasing amount of attached powder as the angle increases.
- (iii) For down-skin surfaces a strongly increasing surface roughness is observed, high amounts of powder particles are attached to the surfaces.

These three categories are illustrated in Fig. 4c.

Based on the captured SEMs of the surface profiles in Fig. 4a the surface roughness parameters R_a and R_z were calculated. An example of a surface profile and the extracted profile is shown in Fig. 5a and the data points and the calculation of R_a and R_z are shown in Fig. 5b. The R_a and R_z values obtained from all the SEMs are shown in Fig. 6. It should be noted that these data are not taken as the average of several measurements but directly from the SEMs presented in Fig. 4a. The main trend observed in Fig. 6 is that the value of R_a and R_z is increasing drastically from 105° to 135° . For values between 0° and 90° , the surface roughness values are slightly decreasing. A decrease in surface roughness when going from 0° to 90° , due to the staircase effect, has also been observed in recent literature [35,36]. The surface roughness for case (i) specimens are dominated by the staircase effect and not equal in different directions. I.e. the surface roughness along the length dimension of the specimens is higher than the surface roughness across the thickness of the specimens (See e.g. 15° in Fig. 4b). In the case of (ii) and (iii), the surface seems to be more uniform in the different directions

¹ https://opencv-python-tutorials.readthedocs.io/en/latest/py_tutorials/py_gui/py_image_display/py_image_display.html

² https://docs.opencv.org/master/d7/d4d/tutorial_py_thresholding.html.

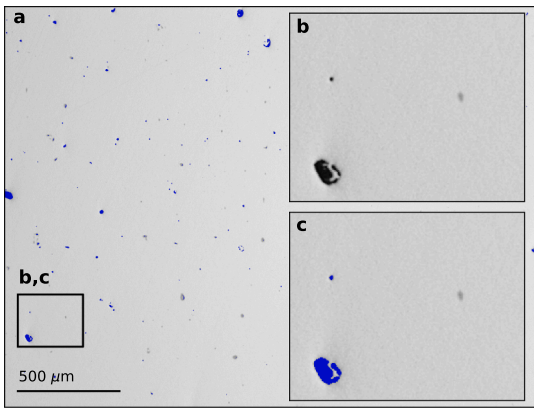


Fig. 7. Example of porosity measurement. (a) Optical micrograph of polished cross section with the detected porosity highlighted in blue. (b) detail of micrograph (c) detail of the micrograph with porosity highlighted.

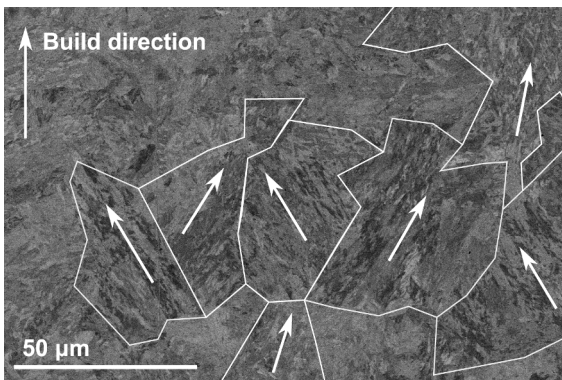


Fig. 8. Microstructure of the material in xz -plane obtained by BSE. Different regions with a clear orientation of the martensite plates are indicated by outlining and arrows.

(See Fig. 4b).

3.2. Porosity

Fig. 7 shows a micrograph of a polished cross-section and the porosity detection. The full micrograph is shown in Fig. 7a and Fig. 7b and c shows a detail of the porosity detection. Note that the black regions with porosity are detected while the grey grinding lines and dirt are neglected. A porosity of $1.68 \pm 0.123\%$ was obtained based on the micrographs.

3.3. Microstructure

The microstructure of the material in the xz -plane is shown in Fig. 8 based on BSE analysis. The analysis displays regions of martensite blocks with plates of similar orientations. These regions are indicated by outlining and the direction of the plates are indicated by arrows in Fig. 8. When the material solidifies in the PBF-LB/M process, the high-atomic density vector $\langle 110 \rangle$ of the primary α -FCC austenite grains aligns with the direction of the heat flux [37], and the primary austenite grains tend to be elongated in the build direction. As the martensite transformation occurs the martensite plate orientation is dictated by the Kurdjumow-Sachs relationship, meaning that the plates can take any one of 24 orientations. This leads to a weak microstructural texture, much less dominant than what can be observed in other materials such as Inconel 718 [38,39] and AlSi10Mg [40].

The Vickers hardness (HV1) of the material was measured in the xz -

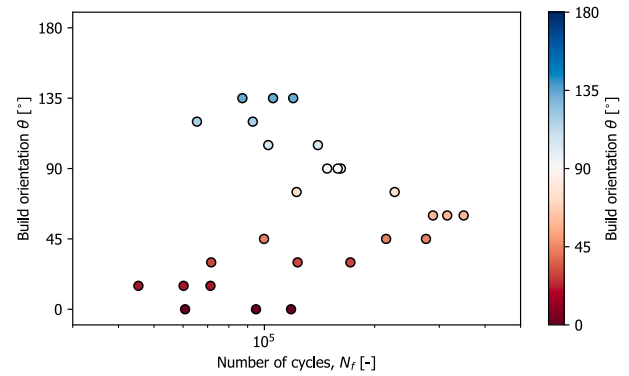


Fig. 9. Fatigue data for different orientations.

Table 1

Specimen dimensions and fatigue data. Build angle θ [°], thickness t [mm], width w [mm], stress range $\Delta\sigma$ [MPa], number of cycles to failure N_f [-].

θ	t	w	$\Delta\sigma$	N_f	Note
0	3.258	6.370	508.9	60760	
0	3.264	6.470	500.1	94862	
0	3.262	6.463	501.0	118234	
15	3.263	6.338	510.7	45314	
15	3.260	6.389	507.1	71265	
15	3.267	6.413	504.1	60186	
30	3.271	6.476	498.6	171628	
30	3.273	6.442	500.9	71586	
30	3.276	6.486	497.1	123178	
45	3.247	6.467	503.0	99761	
45	3.252	6.456	503.1	275975	
45	3.260	6.502	498.3	214804	
60	3.274	6.456	499.7	349644	
60	3.271	6.435	501.8	288333	
60	3.258	6.493	499.3	315357	
75	3.264	6.478	399.6	500000	a
75	3.271	6.500	496.8	122422	
75	3.259	6.498	498.7	226664	
90	3.261	6.620	489.3	148340	
90	3.254	6.547	495.8	161695	
90	3.259	6.529	496.4	158520	
105	3.275	6.557	491.8	139936	
105	3.299	6.531	490.2	102440	
105	3.263	6.388	608.1	66344	b
120	3.252	6.780	479.0	92968	
120	3.245	6.855	474.8	65460	
120	3.248	6.595	789.0	34860	b
135	3.290	7.272	441.5	105578	
135	3.255	7.206	450.3	119832	
135	3.258	7.202	450.1	87085	

a Discontinued.

b Mistake in machining. All sides machined.

plane. The hardness was found to be 634.5 ± 23.4 . It should be noted that this is in the same range as what has been reported by Jagle et al. for laser metal deposition and Damon et al. for PBF-LB for similar heat treatment [17,27]. While Meneghetti et al. reported values of HV 367 for AB PBF-LB/18Ni300 [26].

3.4. Fatigue data

The fatigue data are shown in Fig. 9 and summarized in Table 1. In Fig. 9, the number of cycles is plotted versus the build orientation for specimens tested at the same load level (500 MPa). From this plot a clear trend in the fatigue data is visible; the lowest fatigue life is found close to the horizontal orientation, then the fatigue life is increased when approaching the vertical orientation, and decreasing when entering the down-skin region. The highest fatigue life was found for the 60°-specimens. In general, the down-skin specimens displays lower fatigue life

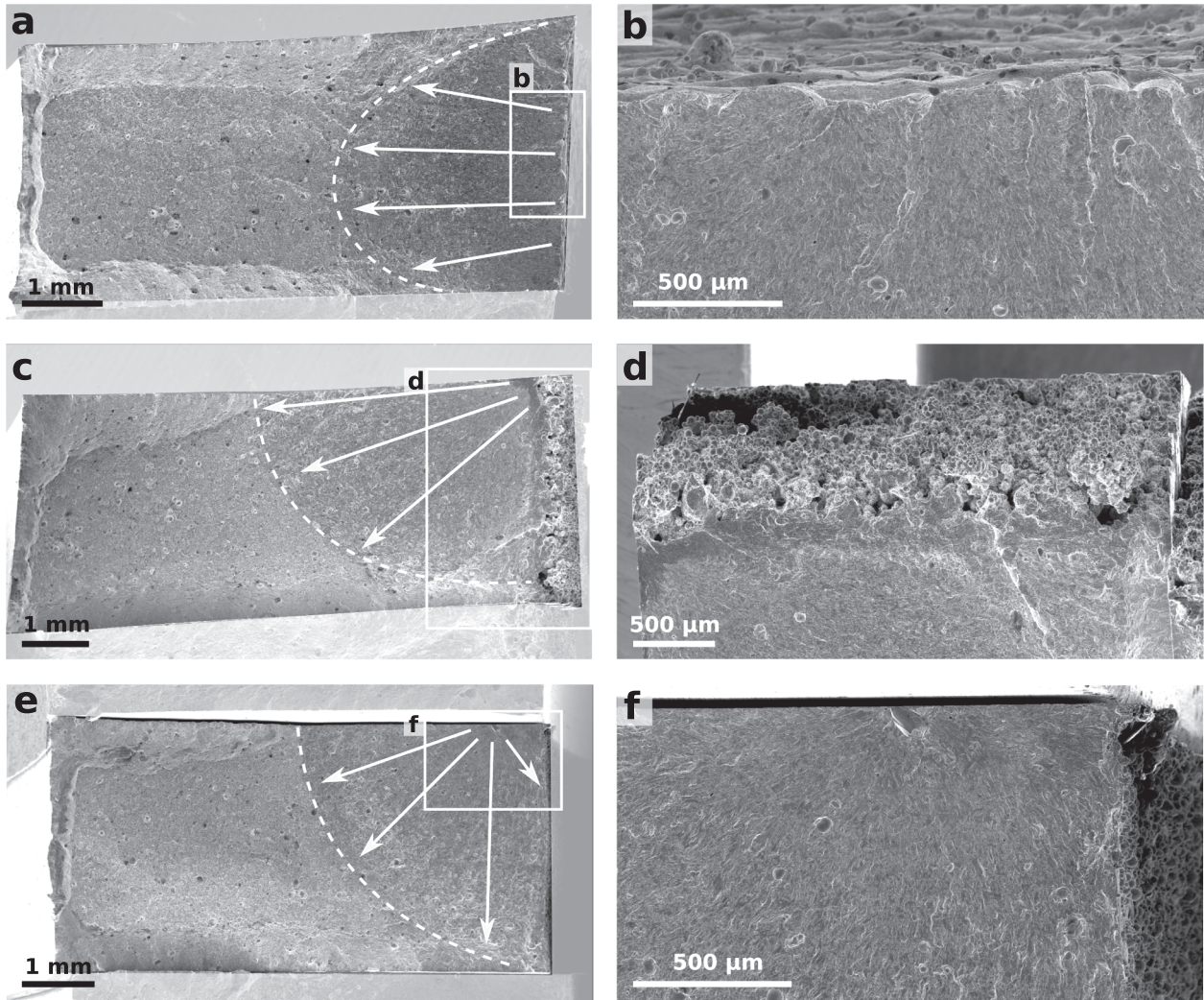


Fig. 10. Fracture surfaces of three different fatigue initiations: (a and b) 0°, fatigue initiation for centre of the AB surface, (c and d) 135°, Fatigue initiation from the corner the AB surface and e and f) 60°, Fatigue initiation from internal defect.

than their up-skin counterparts. Although considering the scatter, the difference is striking, e.g. by comparing 45° and 135°, both orientations display a fatigue life in a similar range. The clearest difference is observed between 60° and 120°.

3.5. Fractography

Fracture surfaces analysed by SEM are shown in Fig. 10. All

specimens that were investigated were found to have fatigue initiating from defects followed by a region of fatigue crack growth and a final rupture zone. The final rupture zone displayed shear lips along the edges. Concerning the fatigue initiation sites, all specimens did not fail from the as-built surfaces; some specimens failed from internal voids and defects close to the as-built surface. Three different fracture surfaces displaying different fatigue initiations are shown in Fig. 10: failure from internal defect, failure from the centre of the as-built surface and failure from the corner of the as-built surface.

In Fig. 10a and b, a specimen built with 0° angle is shown. The specimen has fatigue initiation from the centre of the AB surface. Fatigue initiates from a defect that is ~ 70 μm deep, comparable to the Rz value from Fig. 6, which was measured to be 99.2 μm. In Fig. 10c and d, a specimen built with 135° angle is shown. This specimen is also failing from the AB surface, but fatigue initiated from the corner of the specimen. In this case, the surface roughness, Rz, is higher than the 0° by approximately a factor of 4. In Fig. 10e and f, a specimen built with 60° angle is shown. This specimen does not have fatigue initiation from the AB surface but from a defect close to/at the machined surface. The specimens in this orientation display the highest fatigue life.

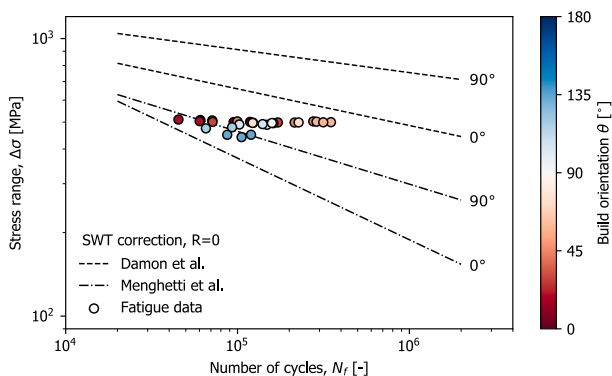


Fig. 11. Comparison of fatigue data.

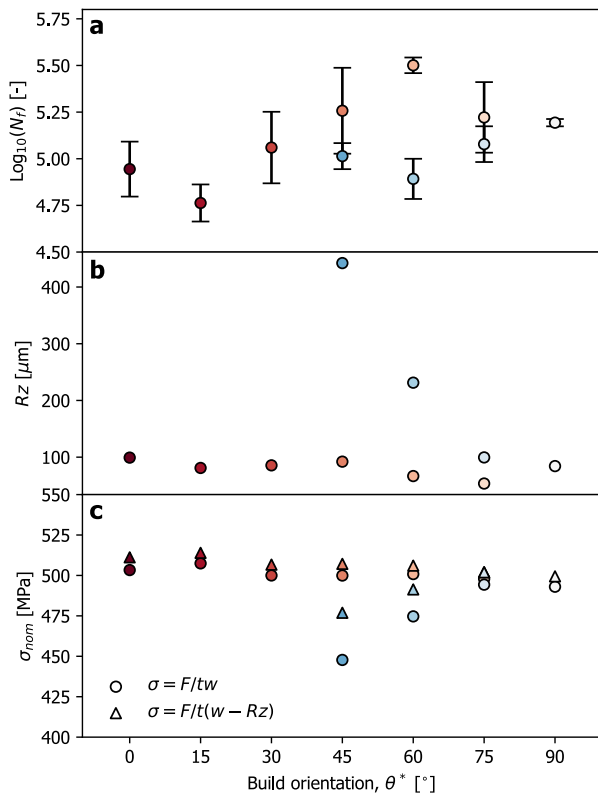


Fig. 12. Comparison of (a) fatigue life, (b) surface roughness and (c) nominal stress.

4. Discussion

4.1. Comparison to fatigue data from the literature

In Fig. 11 the fatigue data obtained in this study are compared to fatigue data on PBF-LB from the literature, represented as regression lines. The stress values of the fatigue data from the present work is taken as the applied load divided by the measured cross-section, listed in Table 1. It should also be noted that the fatigue data from literature were tested at $R = -1$ and were therefore corrected by the Smith-Watson-Topper (SWT) mean stress correction [41]. The SWT mean stress correction is given by

$$\sigma_{ar} = \sigma_{max} \sqrt{\frac{1-R}{2}}, \quad (3)$$

where σ_{ar} is the stress amplitude at $R = -1$ and σ_{max} is the maximum stress during the loading cycle at the given R value. The comparison in Fig. 11 shows that the fatigue data from the present work is in a similar range as the data from the literature. The data from Meneghetti et al. [26] and Damon et al. [27] displayed higher fatigue life for loading in the vertical orientation than the horizontal orientation. A similar trend was observed for the data presented here, specimens close to the horizontal orientation displayed lower fatigue life than the specimens close to the vertical orientation.

From the data in Fig. 11 it is clear that there are variations in the nominal stress due to the specimen dimensions, although the specimens were tested at the same load level.

4.2. Comparison of different build angles

A comparison of the fatigue life, the surface roughness, the nominal stress and the build angle for specimens tested at the same load level is shown in Fig. 12. To compare the up-skin and down-skin surfaces of equal orientation (e.g. 60° and 120°), the build angle is given as

$$\theta^* = \arcsin(\sin(\theta)). \quad (4)$$

Fig. 12a shows a comparison of the build angles and the fatigue life, where the average and standard deviation of the fatigue life is calculated for each angle. The lowest number of cycles was observed for the 15°-specimens, while the fatigue life increased as the built angle increased towards 60°, then decreased from 60° to 135°. In general, when comparing the corresponding build angles, the down-skin specimens have lower fatigue life than the up-skin specimens.

Variations were observed in the specimen dimensions in particular due to the unmachined surfaces. To take into account these variations, the average stress for each build angle is given in Fig. 12c. Based on the dimensions measured by caliper (given values in Table 1), the stress is calculated by $\sigma = F/tw$. The values show that the nominal stress is decreasing for an increasingly down-skin angle. The caliper, however, does not take into account the surface roughness of the specimens and might give a too low value of the nominal stress in the specimens. To take into account the decrease in the cross-sectional area due to the surface roughness, the cross-section was corrected by the R_z values (shown in Fig. 12b), giving a nominal stress calculated by $\sigma = F/t(w - Rz)$. After correction the nominal stress level for the surface roughness, the nominal stress increase slightly for the values between 0° and 105°, while for 120° and 135° the stress increase. It should be noted that correcting by the full value of R_z might be too conservative, but it indicates the possible additional stress level variations. It is also interesting to remark that not only does the surface roughness depend on the build orientation of the surfaces, but also the dimensional tolerances. Deviations in dimensions due to down-skin surfaces has also been

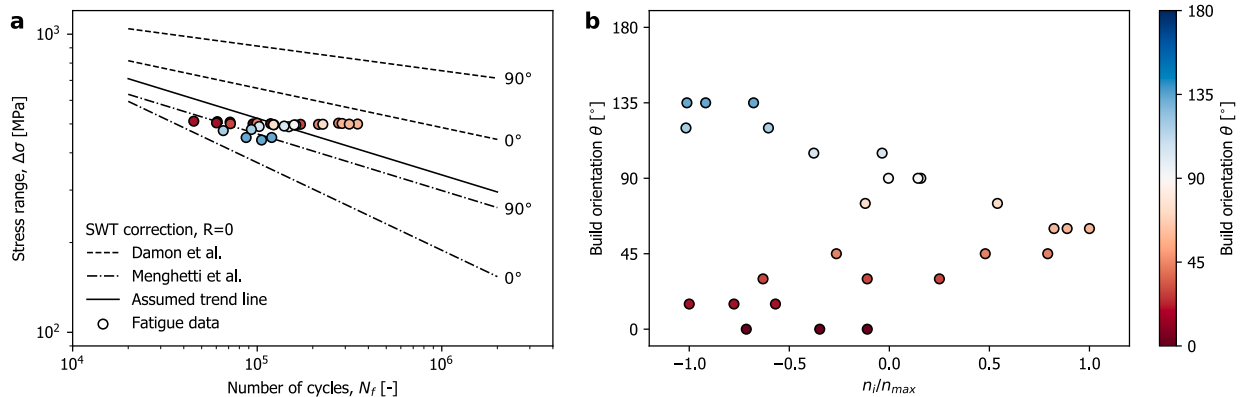


Fig. 13. (a) Comparison of the fatigue data presented in this study and regression lines of the fatigue data of PBF-LB/18Ni300 by Damon et al. and Meneghetti et al. (b) Updated correlation between the build angle and the normalized parameter n_i/n_{max} .

observed by other researchers in e.g. Refs. [42,43].

The fatigue data presented in Fig. 9 and Fig. 12a assumes the load level to be constant. This is, as discussed above, not the case. To correct for the variations in the stress levels, a comparison was made based on the deviation from an assumed fatigue life curve. Fig. 13a shows fatigue data from this study compared with the linear regression of the fatigue data of Meneghetti et al. [26] and Damon et al. [27] (presented previously in Fig. 12). The data from literature are presented in terms of Basquin curves based on power-law fitting of the data. By assuming that the fatigue data presented in this work follows similar trend lines as the data published by Meneghetti et al. [26] and Damon et al. [27], the trend line was described by Basquin's equation. The slope, B , was assumed to have the same value as the Meneghetti et al. [26] 90°-data (as the data are close to this curve). Further, a new "assumed" fatigue life curve was created. The vertical shift, A , of the curve was taken so that the trend line (at 500 MPa) intersects with the mean value of the maximum and the minimum number of cycles at tests done around 500 MPa. The deviation for the assumed fatigue life curve is given by

$$n_{.i} = \log_{-10}(N_{.i}) - \log_{-10} \left(\left(\frac{\sigma_{.i}}{A} \right)^{\frac{1}{B}} \right). \quad (5)$$

Further, the deviation from the regression line is normalized by the maximum value, $n_{.max}$, and the result is shown in Fig. 13b. This comparison gives, perhaps, a more realistic comparison of the corresponding angles, e.g. 45° and 135° or 60° and 120°. Here, the 135° and 120° angle displays lower fatigue life than the 45 and 60 orientations. This comparison between the fatigue life ($n_{.i}/n_{.max}$) confirms that the fatigue life is lower for the down-skin region than for up-skin region.

4.3. Surface morphology

From the correlation between the build angle and surface roughness in Fig. 12b the main shift in the surface roughness conditions is when the surface turns down-skin. Here, the surface roughness increases by over 4 times when comparing the 135° orientation to the general values for the up-skin surfaces. When investigating the morphology of the surfaces in Fig. 4a, no sharp features (notch roots) are observed, contrary to what has been found in the down-skin surface in other studies [10]. In addition to this, the up-skin surfaces display a waviness morphology (the 15° orientation is the extreme). As discussed in Section 3.1, three main surface conditions were identified; high surface roughness for down-skin surface, general surface roughness for vertical orientation and the staircase-like surface for up-skin surfaces. When the surface roughness is governed by the staircase effect, the surface roughness manifests as notches that are defined along the thickness direction of the sample. On the contrary, in the down-skin region, the notches from the surface roughness are not constant along with the thickness direction of the specimens. This could explain why the 15°-specimens, which displays a very distinct staircase surface, has the lowest fatigue life.

5. Conclusions

In the present work, the directional fatigue behaviour of PBF-LB/18Ni300 maraging steel was studied. Specimens with 10 different orientations ranging from 0° to 135° were considered. The following conclusions can be drawn:

- A new test specimen for testing both the up- and down-skin fatigue behaviour of AM metals has been proposed. By machining all sides of a specimen except one, fatigue cracks are guided to initiate from the AB surface.
- The surface roughness was evaluated for surfaces built ranging from 0° (up-skin, horizontal) to 135° (down-skin). The up-skin surfaces

displayed the stair-case effect while the down-skin surfaces displayed high surface roughness.

- The fatigue strength was found to be inferior to wrought 18Ni300 but comparable to other works on AM. Specimens built close to the vertical orientation was found to have longer fatigue life compared to specimens built closer to the horizontal orientation. The same and the opposite trend has been found in recent literature on the same material.
- The specimens with AB up-skin surfaces displayed higher fatigue life than the ones with AB down-skin surface due to the higher surface roughness.

Declaration of Competing Interest

The authors declare that they have no known competing financial interests or personal relationships that could have appeared to influence the work reported in this paper.

Acknowledgement

This work is funded in part by the Norwegian Research Council through Grant No. 248243, and by the TROJAM project in the INTERREG A/ENI program.

The authors would also like to acknowledge Matija Cuzovic for the work done in his master's thesis.

References

- [1] Bourell DL. Perspectives on additive manufacturing. *Annu Rev Mater Res* 2016;46:1–18.
- [2] Wong K, Hernandez K. A review of additive manufacturing. *ISRN Mech Eng* 2012;2012:0–10.
- [3] Wiberg A, Persson J, Olvander J. Design for additive manufacturing – a review of available design methods and software. *Rapid Prototyp J* 2019;25:1080–94.
- [4] Singh S, Ramakrishna S, Singh R. Material issues in additive manufacturing: A review. *J Manuf Process* 2017;25:185–200.
- [5] Lewandowski JJ, Seifi M. Metal additive manufacturing: A review of mechanical properties. *Annu Rev Mater Res* 2016;46:151–86.
- [6] Li C, Liu Z, Fang X, Guo Y. Residual stress in metal additive manufacturing. *Proc CIRP* 2018;71: 348–353. 4th CIRP Conference on Surface Integrity (CSI 2018).
- [7] Megahed M, Mindt H, N'Dri N, Duan H, Desmaison O. Metal additive-manufacturing process and residual stress modeling. *Integr Mater Manuf Innov* 2016;5:61–93.
- [8] Mukherjee T, Zhang W, DebRoy T. An improved prediction of residual stresses and distortion in additive manufacturing. *Comput Mater Sci* 2017;126:360–72.
- [9] McKelvey S, Fatemi A. Surface finish effect on fatigue behavior of forged steel. *Int J Fatigue* 2012;36:130–45.
- [10] Solberg K, Berto F. Notch-defect interaction in additively manufactured inconel 718. *Int J Fatigue* 2019;122:35–45.
- [11] Sanaei N, Fatemi A. Analysis of the effect of internal defects on fatigue performance of additive manufactured metals. *Mater Sci Eng: A* 2020;785:139385.
- [12] Jamshidi P, Aristizabal M, Kong W, Villapun V, Cox SC, Grover LM, Attallah MM. Selective laser melting of ti-6al-4v: The impact of post-processing on the tensile, fatigue and biological properties for medical implant applications. *Materials* 2020;13:2813.
- [13] Molaei R, Fatemi A, Phan N. Significance of hot isostatic pressing (hip) on multiaxial deformation and fatigue behaviors of additive manufactured ti-6al-4v including build orientation and surface roughness effects. *Int J Fatigue* 2018;117: 352–70.
- [14] Tamas-Williams S, Withers PJ, Todd I, Prangnell PB. The effectiveness of hot isostatic pressing for closing porosity in titanium parts manufactured by selective electron beam melting. *Metall Mater Trans A* 2016;47:1939–46.
- [15] Crococolo D, Agostinis M, Fini S, Olmi G, Robusto F, Kostić S, Vranić A, Bogojević N. Fatigue response of as-built dmls maraging steel and effects of aging, machining, and peening treatments. *Metals* 2018;8(7):505.
- [16] Wan H-Y, Zhou Z-J, Li C-P, Chen G-F, Zhang G-P. Enhancing fatigue strength of selective laser melting-fabricated inconel 718 by tailoring heat treatment route. *Adv Eng Mater* 2018;20:1800307.
- [17] Jäggle E, Sheng Z, Kürsteiner P, Cyclok S, Weisheit A, Raabe D, Requena G. Comparison of maraging steel micro- and nanostructure produced conventionally and by laser additive manufacturing. *Materials* 2017;10.
- [18] Turk C, Zunko H, Aumayr C, Leitner H, Kapp M. Advances in maraging steels for additive manufacturing. *BHM Berg- und Hüttenmännische Monatshefte* 2019;164.
- [19] Bajaj P, Hariharan A, Kini A, Kürsteiner P, Raabe D, Jäggle E. Steels in additive manufacturing: A review of their microstructure and properties. *Mater Sci Eng: A* 2020;772:138633.

- [20] Kempen K, Yasa E, Thijs L, Kruth J-P, Humbeeck J. Microstructure and mechanical properties of selective laser melted 18ni300 steel. *Phys Proc* 2011;12:255–63.
- [21] Becker TH, Dimitrov D. The achievable mechanical properties of slm produced maraging steel 300 components. *Rapid Prototyp J* 2016;22:487–94.
- [22] Wang B, Zhang P, Duan Q, Zhang Z, Yang H, Li X, Zhang Z. Optimizing the fatigue strength of 18ni maraging steel through ageing treatment. *Mater Sci Eng: A* 2017; 707:674–88.
- [23] Van Swam LF, Pelloux RM, Grant NJ. Fatigue behavior of maraging steel 300. *Metall Trans A* 1975;6:45–54.
- [24] Meneghetti G, Rigon D, Cozzi D, Waldhauser W, Dabalà M. Influence of build orientation on static and axial fatigue properties of maraging steel specimens produced by additive manufacturing. *Proc Struct Integr* 2017;7:149–57.
- [25] Crocchio D, De Agostinis M, Fini S, Olmi G, Vranic A, Ciric-Kostic S. Influence of the build orientation on the fatigue strength of eos maraging steel produced by additive metal machine. *Fatigue Fract Eng Mater Struct* 2016;39:637–47.
- [26] Meneghetti G, Rigon D, Gennari C. An analysis of defects influence on axial fatigue strength of maraging steel specimens produced by additive manufacturing. *Int J Fatigue* 2019;118:54–64.
- [27] Damon J, Hanemann T, Dietrich S, Graf G, Lang K-H, Schulze V. Orientation dependent fatigue performance and mechanisms of selective laser melted maraging steel x3nicomoti18-9-5. *Int J Fatigue* 2019;127:395–402.
- [28] Yadollahi A, Shamsaei N, Thompson SM, Elwany A, Bian L. Effects of building orientation and heat treatment on fatigue behavior of selective laser melted 17–4 ph stainless steel. *Int J Fatigue* 2017;94:218–35.
- [29] Herzog D, Seyda V, Wycisk E, Emmelmann C. Additive manufacturing of metals. *Acta Mater* 2016;117.
- [30] Riemer A, Leuders S, Thöne M, Richard H, Tröster T, Niendorf T. On the fatigue crack growth behavior in 316l stainless steel manufactured by selective laser melting. *Eng Fract Mech* 2014;120:15–25.
- [31] Mower TM, Long MJ. Mechanical behavior of additive manufactured, powder-bed laser-fused materials. *Mater Sci Eng: A* 2016;651:198–213.
- [32] Edwards P, Ramulu M. Fatigue performance evaluation of selective laser melted ti–6al–4v. *Mater Sci Eng: A* 2014;598:327–37.
- [33] Johannes Lindecke PN, Blunk H, Wenzl J-P, Möller M, Emmelmann C. Optimization of support structures for the laser additive manufacturing of tial6v4 parts. *Proc CIRP* 2018;74:53–8. 10th CIRP Conference on Photonic Technologies [LANE 2018].
- [34] Emmelmann C, Herzog D, Kranz J. 10 - design for laser additive manufacturing. In: Brandt M, editor. *Laser Additive Manufacturing*, Woodhead Publishing Series in Electronic and Optical Materials. Woodhead Publishing; 2017. p. 259–79.
- [35] Strano G, Hao L, Everson RM, Evans KE. Surface roughness analysis, modelling and prediction in selective laser melting. *J Mater Process Technol* 2013;213:589–97.
- [36] Hovig EW, Azar AS, Sunding MF, Andreassen E, Sørby K. High cycle fatigue life estimation of materials processed by laser powder bed fusion. *Fatigue Fract Eng Mater Struct* 2019;42:1454–66.
- [37] Azar AS, Østby E, Akselsen OM. Effect of hyperbaric chamber gas on transformation texture of the API-X70 pipeline weld metal. *Metall Mater Trans A: Phys Metall Mater Sci*; 2012.
- [38] Chlebus E, Gruber K, Kuźnicka B, Kurzac J, Kurzynowski T. Effect of heat treatment on the microstructure and mechanical properties of Inconel 718 processed by selective laser melting. *Mater Sci Eng A* 2015;639:647–55.
- [39] Hovig W, Azar AS, Grytten F, Sørby K, Andreassen E. Determination of anisotropic mechanical properties for materials processed by laser powder bed fusion. *Adv Mater Sci Eng* 2018;2018.
- [40] Brandl E, Heckenberger U, Holzinger V, Buchbinder D. Additive manufactured AlSi10Mg samples using Selective Laser Melting (SLM): Microstructure, high cycle fatigue, and fracture behavior. *Mater Des* 2012;34:159–69.
- [41] Smith KN, Watson P, Topper TH. A stress strain function for the fatigue of metals. *J Mater* 1970;5:767–78.
- [42] Andreau O, Pessard E, Koutiri I, Peyre P, Saintier N. Influence of the position and size of various deterministic defects on the high cycle fatigue resistance of a 316l steel manufactured by laser powder bed fusion. *Int J Fatigue* 2021;143:105930.
- [43] Matache G, Paraschiv A, Condruz R. Edge and corner effects in selective laser melting of in 625 alloy. *Manuf Rev* 2020;7:8.